photonics

MDPI

Article

Hybrid 4DPPM-DQPSK Modulation for Terrestrial Free-Space Optical Links Under Atmospheric Turbulence

Xinning Huang [1,*], Zilong Che [1] and Junxia Wu [2]

[1] School of Physical Science and Technology, Yangzhou University, Yangzhou 225002, China; mz120230576@stu.yzu.edu.cn
[2] Xi'an Institute of Optics and Precision Mechanics, Chinese Academy of Sciences, Xi'an 710119, China; wujunxia@opt.ac.cn
* Correspondence: huangxinning@yzu.edu.cn

Abstract

Terrestrial free-space laser communication will play a pivotal role in future 6G networks, owing to its high bandwidth and low latency advantages. However, atmospheric turbulence degrades link performance due to intensity scintillation and phase distortion. This paper proposes a hybrid modulation scheme that combines differential pulse position modulation (DPPM) with differential quadrature phase-shift keying (DQPSK). The scheme exploits the power efficiency of DPPM and the spectral efficiency of DQPSK, while differential phase detection eliminates the need for carrier recovery and enhances robustness to phase noise. A theoretical bit error rate (BER) model is derived and validated under Gamma–Gamma and Log-normal turbulence channels. Results show that the 4DPPM-DQPSK configuration achieves BER up to several orders of magnitude lower than standalone DPPM or DQPSK under weak-to-moderate turbulence, and improves spectral efficiency by 50% relative to 4DPPM. Packet error rate analysis further confirms its reliability for high-capacity terrestrial FSO links.

Keywords: atmospheric turbulence; bit error rate; hybrid modulation; terrestrial FSO

1. Introduction

Free-space optical communication (FSO) offers compelling advantages over traditional radio-frequency systems, including higher data rates, lower latency, license-free spectrum, and significant reductions in size, weight, and power (SWaP) requirements [1–5]. These merits position FSO as a cornerstone for next-generation communication networks. Numerous initiatives, including Low Earth Orbit (LEO) constellations such as Starlink [6], Geostationary Earth Orbit (GEO) satellites such as Europe's EDRS [7], deep-space missions such as NASA's DSOC [8] and LEO satellite-assisted optical communication systems [9], have successfully demonstrated the feasibility of FSO technology.

Despite their potential, FSO systems face significant deployment challenges, particularly the detrimental effects of atmospheric turbulence on the transmission links. Turbulence can induce intensity scintillation and beam wandering [10], degrading transmission performance and potentially leading to link outages. Various approaches have been proposed to mitigate the turbulence effects. Adaptive optics (AO) [11,12] can compensate for wavefront distortion, but its system is often somewhat bulky and the correction bandwidth is typically limited to weak-to-moderate turbulence. Structured light using orbital angular momentum (OAM) [13] offers an alternative approach, yet requires complex generation

Check for updates

Received: 21 May 2026
Revised: 5 June 2026
Accepted: 8 June 2026
Published: 9 June 2026

Copyright: © 2026 by the authors. Licensee MDPI, Basel, Switzerland. This article is an open access article distributed under the terms and conditions of the Creative Commons Attribution (CC BY) license.

and detection schemes. Artificial intelligence (AI)-based turbulence prediction [14] has emerged more recently, though practical deployment still requires further optimization for accuracy and latency. Multi-aperture receivers with maximal-ratio combining (MRC) algorithms [15] and multi-mode fiber-based coherent combining [16] represent hardware-intensive solutions that demand specialized optical components. In addition, transmit laser/receive antenna selection also provides effective solutions for mitigating atmospheric turbulence [17,18]. In summary, most existing mitigation strategies face trade-offs among complexity, bandwidth, and turbulence regime applicability.

The m-ary pulse position modulation (mPPM) format, known for its high receiver sensitivity and power efficiency, has been widely adopted in deep-space optical communication and exhibits strong immunity to atmospheric turbulence [19–22]. However, its low spectral efficiency (typically limiting data rates below 1 Gb/s) restricts high-capacity applications. Consequently, hybrid modulation techniques such as QAM-mPPM, PPM-DPSK, and PPM-QPSK have been proposed to enhance spectral efficiency (SE) while preserving anti-turbulence characteristics [23–25]. A common limitation in existing studies is that anti-turbulence performance is often evaluated under a single turbulence model and thus lacks universality. Moreover, absolute phase modulation components in these hybrids remain sensitive to turbulence-induced phase perturbations, undermining the overall system robustness.

To address these issues, this paper proposes a novel dual-differential hybrid modulation scheme, termed m-ary differential pulse position modulation–differential quadrature phase-shift keying (mDPPM-DQPSK). This format aims to deliver high-capacity data transmission alongside superior anti-turbulence performance for FSO systems. The key innovations and contributions of this work are summarized as follows:

1. A hybrid modulation architecture that combines differential pulse position encoding and differential phase-shift keying is proposed. By exploiting the power efficiency of DPPM and the high spectral efficiency of DQPSK, the scheme achieves simultaneous mitigation of intensity scintillation and slow-varying phase distortion via differential detection, eliminating the need for carrier recovery and absolute phase synchronization.
2. A unified theoretical BER model for mDPPM-DQPSK is derived for the first time under both Gamma–Gamma and Log-normal turbulence distributions, covering weak to moderate turbulence conditions. This model provides an accurate theoretical foundation for system performance evaluation and optimization.
3. Extensive numerical simulations demonstrate that the 4DPPM-DQPSK configuration outperforms standalone DPPM and DQPSK by several orders of magnitude in BER under weak-to-moderate turbulence. Packet error rate (PER) analysis further validates its reliability for long-distance, high-capacity terrestrial FSO links.

The remainder of this paper is organized as follows: Section 2 introduces the modulation principle, spectral efficiency analysis, and theoretical BER derivation of the proposed mDPPM-DQPSK scheme. Section 3 presents the anti-turbulence performance under Gamma–Gamma and Log-normal turbulence channels and gives the packet error rate analysis. Finally, Section 4 discusses the obtained results and Section 5 concludes the paper.

2. Materials and Methods

In m-ary PPM, information is encoded in the position of a single pulse within a symbol duration T_s, which is divided into m equal time slots. A group of n bits (where $n = \log_2 m$) is mapped onto one active slot, with the remaining slots kept empty, resulting in a symbol carrying n bits. This process, however, consumes significant bandwidth and requires strict symbol synchronization at the receiver. To improve SE and release synchronization constraints, differential PPM (DPPM) is introduced by eliminating all empty slots following

the pulse. The presence of an optical pulse directly signifies the end of the current symbol and the start of the next.

In QPSK modulation, the 2π phase period of the laser carrier is partitioned into four phases, with each 2-bit sequence mapped onto one of these absolute phase states. However, random phase fluctuations caused by turbulence can lead to phase ambiguity, deteriorating its BER performance. DQPSK employs a differential encoding scheme, where information is encoded in the phase difference between consecutive symbols. Since phase fluctuations induced by atmospheric turbulence typically manifest as slow variation, with coherent time being much longer than the symbol period, such noise can be suppressed through adjacent symbol subtraction during the differential detection [26]. Therefore, the turbulence resistance of DQPSK is improved while maintaining the same SE, endowing the FSO links with strong robustness.

In the proposed mDPPM-DQPSK format with modulation order $m = 4$, the input bit stream is partitioned into 4-bit groups. The first 2 bits determine the pulse position among four possible time slots via DPPM encoding. The remaining 2 bits are differentially encoded and mapped to four possible phase difference ($\pi/4$, $3\pi/4$, $5\pi/4$, or $7\pi/4$) of that pulse relative to the preceding one via DQPSK modulation. Finally, an optical pulse sequence carrying both pulse position and phase information is obtained. The corresponding transmitter architecture is shown in Figure 1a; an IQ modulator is employed to simultaneously encode the pulse position and phase information. The IQ modulator consists of two nested Mach–Zehnder modulators (MZMs) with a 90-degree phase offset between their outputs, enabling independent control of the in-phase (I) and quadrature (Q) components of the optical field. By setting appropriate (I, Q) drive voltages for each time slot, the output amplitude (proportional to $\sqrt{I^2 + Q^2}$) and phase (arctan(Q/I)) can be independently controlled. For empty slots, (I, Q) = (0, 0) produces zero optical output; for active slots, the (I, Q) values are set to generate the required DQPSK phase state. This pre-encoding approach avoids the need for optical synchronization between the DPPM and DQPSK modulation stages. At the receiver, differential detection is adopted for demodulation after clock recovery and the original data are obtained after the parallel-to-series conversion, as shown in Figure 1b. The 4DPPM-DQPSK modulation process is also illustrated in Figure 1c.

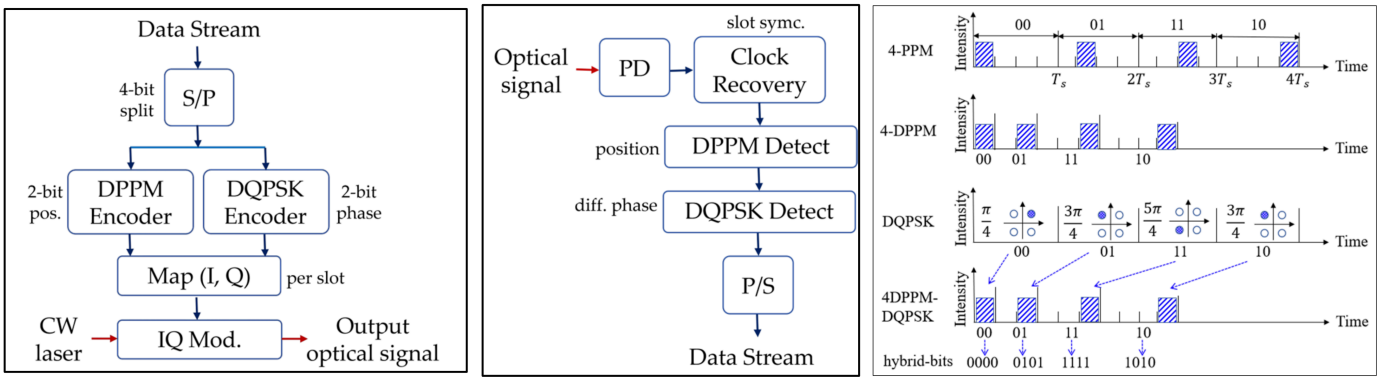


Figure 1. (**a**) Transmitter, (**b**) receiver architecture and (**c**) the modulation process of the proposed mDPPM-DQPSK scheme. S/P: series-to-parallel conversion, Mod.: modulator, PD: photodetector, P/S: parallel-to-series conversion.

A potential concern is whether the introduction of differential phase modulation negates the inherent robustness of pulse position-based intensity detection. In the proposed scheme, these two modulation dimensions operate in orthogonal physical domains. The DPPM component is detected via intensity thresholding—the presence or absence of a

pulse in each time slot—which remains unaffected by the optical phase state. The DQPSK component, conversely, is recovered through differential phase comparison between consecutive pulses, which inherently rejects common-mode phase perturbations. Because DPPM's variable-length symbol structure naturally partitions the received signal into short pulse intervals, each DQPSK phase comparison occurs within a temporal window significantly shorter than the typical turbulence coherence time (which is on the order of milliseconds for atmospheric channels). Under these conditions, the differential phase approximation holds even under moderate turbulence where absolute phase varies considerably. Thus, rather than compromising PPM's robustness, the DQPSK layer exploits an independent physical dimension (relative phase) that is largely decoupled from the intensity scintillation that DPPM mitigates, yielding a true orthogonality in error mechanisms.

2.1. Spectral Efficiency

The bandwidth expansion factor (BWEF) is commonly used to evaluate the SE of a modulation scheme, which is the inverse of SE. The BWEF for mDPPM, DQPSK, and the hybrid mDPPM-DQPSK are calculated as follows [27]:

$$BWEF_{mDPPM} = \frac{L}{log_2 m} \tag{1}$$

$$BWEF_{mDPPM} = \frac{1}{2} \tag{2}$$

$$BWEF_{mDPPM-DQPSK} = \frac{L}{log_2 m + 2} \tag{3}$$

In Equations (1) and (3), $L = (m+1)/2$ is the average symbol duration for mDPPM. Figure 2 plots the BWEFs as a function of modulation order m, where smaller BWEF indicates higher SE. For DQPSK, the BWEF remains constant at 0.5. The proposed mDPPM-DQPSK hybrid modulation consistently exhibits higher SE (lower BWEF) than mDPPM alone. Setting $m = 4$, the BWEF of hybrid 4DPPM-DQPSK is 0.625, compared to 1.25 for standalone 4DPPM, confirming its intended SE improvement. Although the proposed hybrid shows higher BWEF than DQPSK, its superior anti-turbulence performance, discussed subsequently, makes this trade-off worthwhile.

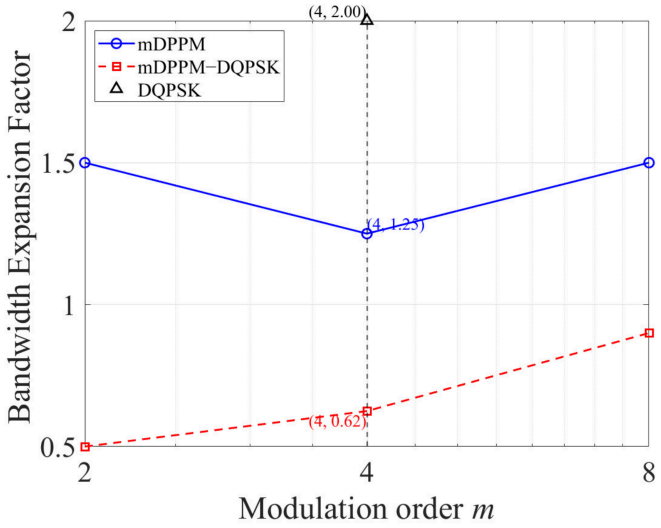


Figure 2. Theoretical BWEF of mDPPM-DQPSK compared with single mDPPM and DQPSK. A smaller BWEF indicates higher spectral efficiency.

2.2. BER Model

To the best of our knowledge, this study theoretically derives the BER model of the proposed mDPPM-DQPSK modulation scheme for the first time. The theoretical BER for DQPSK is given by [28]:

$$BER_{DQPSK} = Q_1(a,b) - \frac{1}{2} I_0(ab) \cdot exp\left[-\frac{1}{2}\left(a^2 + b^2\right)\right] \tag{4}$$

where $Q_1(\cdot)$ is the first-order Marcum Q-function, $I_0(\cdot)$ is the zero-order modified Bessel function of the first kind, and the parameters a and b are expressed as [29]:

$$a = \sqrt{2\gamma_b\left(1 - \sqrt{1/2}\right)}, b = \sqrt{2\gamma_b\left(1 + \sqrt{1/2}\right)} \tag{5}$$

where γ_b denotes the signal-to-noise ratio (SNR) per bit.

For the mDPPM format, the symbol error rate (SER) can be approximated by considering the probability of erroneous slot detection. Since DPPM symbols have variable lengths, we adopt the truncated union bound assuming perfect slot synchronization. The SER is expressed as [29]:

$$SER_{mDPPM} \approx \frac{m}{2} \cdot erfc(\gamma_s/4) \tag{6}$$

where $\boldsymbol{\gamma_s}$ is the SNR per symbol, and $\boldsymbol{erfc}(\cdot)$ is the complementary error function. The corresponding BER for the mDPPM component is [30]:

$$\boldsymbol{BER_{mDPPM} = \frac{m/2}{m-1} \cdot SER_{mDPPM} \approx \frac{m^2}{4(m-1)} \cdot erfc\left(\frac{\gamma_s}{4}\right)} \tag{7}$$

By integrating the error contributions from both modulation components, the overall BER of the hybrid mDPPM-DQPSK modulation can be expressed as a weighted sum of two mutually exclusive error events: when the pulse position is incorrectly detected, both the $log_2 m$ position bits and the p = 2 phase bits carried by that pulse are compromised, and when the pulse position is correctly identified but the differential phase detection fails, only the p = 2 phase bits are affected. Consequently, the composite BER is formulated as follows [31]:

$$BER_{mDPPM-DQPSK} = \frac{log_2 m}{log_2 m + p} \cdot BER_{mDPPM} + \frac{p}{log_2 m + p} \cdot BER_{DQPSK} \cdot (1 - SER_{mDPPM}) \tag{8}$$

where p = 2 denotes the number of bits contributed by the DQPSK component. This formulation assumes that DPPM position errors and DQPSK phase errors are statistically independent, which is a reasonable approximation given the orthogonal nature of the time slot and phase detection mechanisms. Meanwhile, it should be noted that the derived BER model assumes ideal slot synchronization and statistically independent slot errors. However, due to the variable symbol length of DPPM, a single slot error may cause symbol misalignment and propagate to subsequent symbols, introducing error correlation not captured in the present BER formulation. This error propagation effect is partially addressed through the PER analysis in Section 3, which accounts for burst errors within a packet. We further justify the independence assumption as follows: the DPPM slot-position decision is based on intensity threshold detection, where the decision statistic is the integrated photocurrent over each slot interval. The DQPSK differential phase decision, in contrast, relies on the relative phase between two consecutive pulse slots, which is extracted from the same photocurrent waveform but through a fundamentally different signal-processing path (phase comparison vs. amplitude thresholding). The noise components affecting these two decision processes—shot noise in the intensity domain

and phase noise in the angular domain—are statistically independent under the additive white Gaussian noise (AWGN) model commonly adopted in FSO analysis [9,32]. Therefore, the joint error probability factorizes as assumed in Equation (8). However, under strong turbulence where intensity scintillation and phase fluctuations become correlated through the same atmospheric eddies, this independence assumption may become less accurate. A more rigorous joint statistical model that captures the cross-correlation between amplitude and phase errors would be required for a complete characterization under all turbulence regimes, and we identify this as an important direction for future work.

The calculated BER curves for the hybrid mDPPM-DQPSK format are depicted in Figure 3. The BER performance improves with increasing SNR. For a given BER level, higher modulation order m requires lower SNR due to the increased power efficiency of DPPM, albeit at the cost of reduced spectral efficiency. These results provide valuable references for FSO system design where trade-offs between BER, SNR and SE must be carefully balanced. For instance, at a BER level of 10^{-7}, the required SNR for 4DPPM-DQPSK is approximately 11.75 dB.

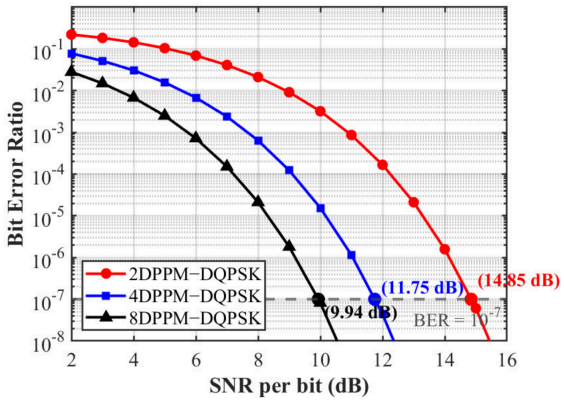


Figure 3. Theoretical BER curves of hybrid mDPPM-DQPSK with different modulation orders under ideal channel conditions.

It is worth addressing a common concern regarding hybrid modulation schemes: whether combining two modulations can yield BER superior to either constituent. In previously reported hybrids such as PPM-QPSK or QAM-mPPM, the phase modulation component typically employs absolute phase encoding, which reintroduces phase sensitivity that undermines PPM's intensity detection advantage. The proposed mDPPM-DQPSK scheme differs fundamentally in that both the pulse position and the phase modulation layers adopt differential encoding. This dual-differential architecture creates a mutual reinforcement effect: DPPM's variable-length structure confines each DQPSK phase comparison to a short temporal window bounded by the DPPM symbol duration—far shorter than the turbulence coherence time—while DQPSK's differential detection inherently cancels slow-varying phase noise through adjacent symbol subtraction. The result is a scheme where the two modulation dimensions operate in complementary error spaces, enabling the observed BER improvements.

3. Results

Atmospheric turbulence induces random fluctuations in received optical power, degrading system performance or even completely interrupting the data transmission links.

The average BER for FSO systems is obtained by averaging the conditional BER over the turbulence-induced fading statistics [33]:

$$P = \int_0^\infty BER \cdot f(I) dI \tag{9}$$

where $f(I)$ is the probability density function (PDF) of the received optical intensity I propagating through the turbulent channels.

In this section, simulations are conducted based on the theoretical BER model and the average BER expression derived above. The average BER is evaluated via numerical integration. In the averaging procedure, the instantaneous electrical SNR per bit is related to the received optical intensity I as $\gamma_b = \gamma_0 \cdot I^2$, where γ_0 is the SNR under zero turbulence ($I = 1$). This quadratic relationship arises because the photodetected electrical signal power scales as the square of the received optical field amplitude. Consequently, turbulence-induced intensity fading I directly modulates the effective electrical SNR, and the average BER is obtained by integrating the conditional BER over the PDF of I, as expressed in Equation (9). The numerical integration employs adaptive Gauss–Kronrod quadrature with 10^6 samples to ensure convergence to verify the validity of the theoretical model under turbulent channel conditions.

3.1. Gamma–Gamma Distribution

The Gamma–Gamma distribution model is first considered due to its wide applicability from weak to strong turbulence. The PDF of the received optical intensity under Gamma–Gamma distribution is [34]:

$$f(I) = \frac{2(\alpha\beta)^{\frac{\alpha+\beta}{2}}}{\Gamma(\alpha)\Gamma(\beta)} \cdot I^{\frac{\alpha+\beta}{2}-1} \cdot K_{\alpha-\beta}\left(2\sqrt{\alpha\beta I}\right), \; I \geq 0 \tag{10}$$

where I is the optical intensity fading caused by the turbulence, $K_\nu(\cdot)$ is the modified Bessel function of the second kind, $\Gamma(\cdot)$ is the Gamma function, and α and β represent the effective numbers of large-scale and small-scale scatterers, given by [34]:

$$\alpha = \left[exp\left(\frac{0.49\chi^2}{\left(1 + 0.18d^2 + 0.56\chi^{12/5}\right)^{\frac{7}{6}}} \right) - 1 \right]^{-1} \tag{11}$$

$$\beta = \left[exp\left(\frac{0.51\chi^2\left(1 + 0.69\chi^{12/5}\right)^{\frac{-5}{6}}}{\left(1 + 0.9d^2 + 0.62d^2\chi^{12/5}\right)^{\frac{5}{6}}} \right) - 1 \right]^{-1} \tag{12}$$

with $\chi = 1.23C_n^2 \cdot k^{7/6} \cdot L^{11/6}$ (namely Rytov variance σ_R^2), and $d = \sqrt{kD^2/4L}$. Here C_n^2 is the refractive index structure constant, $k = 2\pi/\lambda$ is the wave number, λ is the wavelength, D is the receiver aperture diameter and L is the transmission distance.

Substituting the derived BER model and the Gamma–Gamma PDF into the average BER formula (9), we simulated the average BER for 4DPPM-DQPSK using MATLAB (R2022a), with parameters $\lambda = 1550$ nm and $D = 0.05$ m.

First, with a fixed transmission distance $L = 800$ m, we examined the impact of the turbulence strength by setting C_n^2 to 8.2×10^{-15} $m^{-2/3}$ (weak), 1.4×10^{-14} $m^{-2/3}$ (moderate) and 4×10^{-13} $m^{-2/3}$ (strong), respectively. The turbulence strengths expressed via C_n^2 can be equivalently characterized by the Rytov variance σ_R^2, and for the adopted values, the weak regime corresponds to $\sigma_R^2 < 1$, moderate to $\sigma_R^2 \sim 1$, and strong to $\sigma_R^2 > 1$ [35]. The results are shown in Figure 4. At a reference SNR of 12 dB, the proposed 4DPPM-DQPSK

consistently exhibits superior anti-turbulence performance compared to single-modulated formats. In weak (Figure 4a) and moderate (Figure 4b) turbulence, BERs of 4DPPM-DQPSK are 7.2×10^{-18} and 5.98×10^{-18}, nearly three orders of magnitude lower than DQPSK. Under strong (Figure 4c) turbulence, its BER is 4.09×10^{-8}, approximately five orders of magnitude lower than DQPSK and three orders of magnitude lower than DPPM, verifying its higher reliability. Notably, DQPSK shows worse BER performance than DPPM in strong turbulence, verifying that the compensation capability of differential detection reaches the performance limit under extreme phase perturbations. Nevertheless, the proposed 4DPPM-DQPSK hybrid scheme still outperforms both individual schemes significantly. This is because the DPPM provides a fundamental robustness floor against intensity disturbances, while the DQPSK offers SE gains under weak and moderate turbulence regimes. It should be noted that these results represent analytical evaluations based on the derived theoretical model under idealized assumptions (perfect slot synchronization, AWGN-limited detection, and no background radiation). Practical implementation penalties—including thermal noise, dark current, shot noise, and finite photodetector bandwidth—would moderately degrade the absolute BER values. However, the relative performance advantage of the proposed hybrid scheme over standalone DPPM and DQPSK is expected to persist under practical receiver conditions, as all schemes share common receiver impairments. The key conclusion—that the dual-differential architecture enables BER superior to either constituent modulation—is supported by the orthogonal error mechanism argument rather than by optimistic parameter choices. Furthermore, the phase noise and intensity scintillation are jointly accounted for in the average BER framework: scintillation effects enter through the turbulence PDF $f(I)$, while phase noise robustness is demonstrated separately through the Monte Carlo Wiener phase noise simulations in Section 3.4.

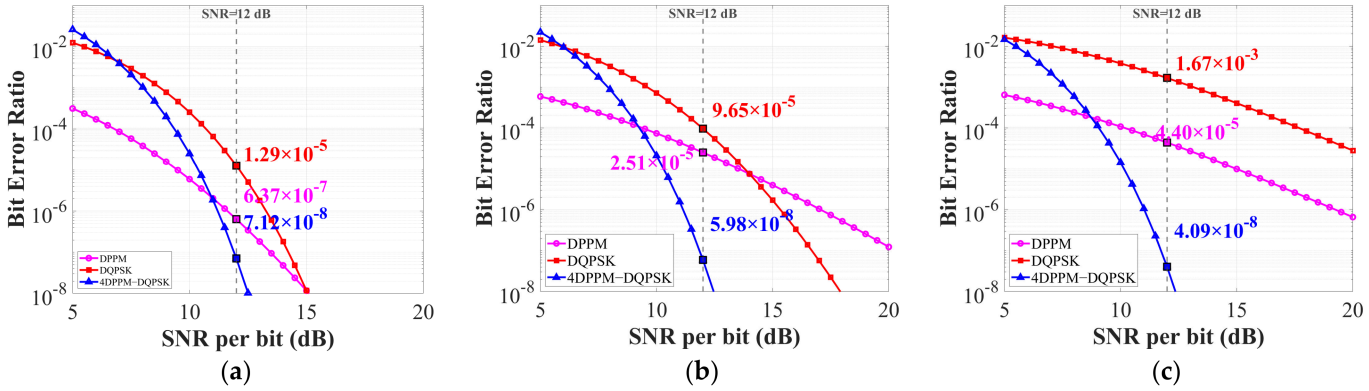


Figure 4. Average BER performance of 4DPPM-DQPSK, DPPM and DQPSK under (**a**) weak, (**b**) moderate and (**c**) strong turbulence regimes based on the Gamma–Gamma model.

Next, we analyzed the impact of propagation distance on the average BER performances. Setting $C_n^2 = 8.2 \times 10^{-15}$ m$^{-2/3}$ (weak turbulence) and distances L = 2000 m, 5000 m and 8500 m, the average BER curves are shown in Figure 5. The 4DPPM-DQPSK scheme consistently outperforms the single-modulated formats, with advantages becoming more pronounced as distance increases. At SNR = 12 dB, after L = 2000 m propagation (Figure 5a), the BER of 4DPPM-DQPSK is 7.34×10^{-8}, three and four orders of magnitude lower than DPPM and DQPSK, respectively. At L = 8500 m propagation (Figure 5c), its superiority over DPPM further expands to five orders of magnitude. These results confirm the applicability of 4DPPM-DQPSK for long-distance links. Furthermore, Figure 5 shows that as transmission distance increases, DPPM performance degrades more rapidly than DQPSK, which is attributed to the inherent receiving sensitivity advantage of DQPSK's coherent detection mechanisms.

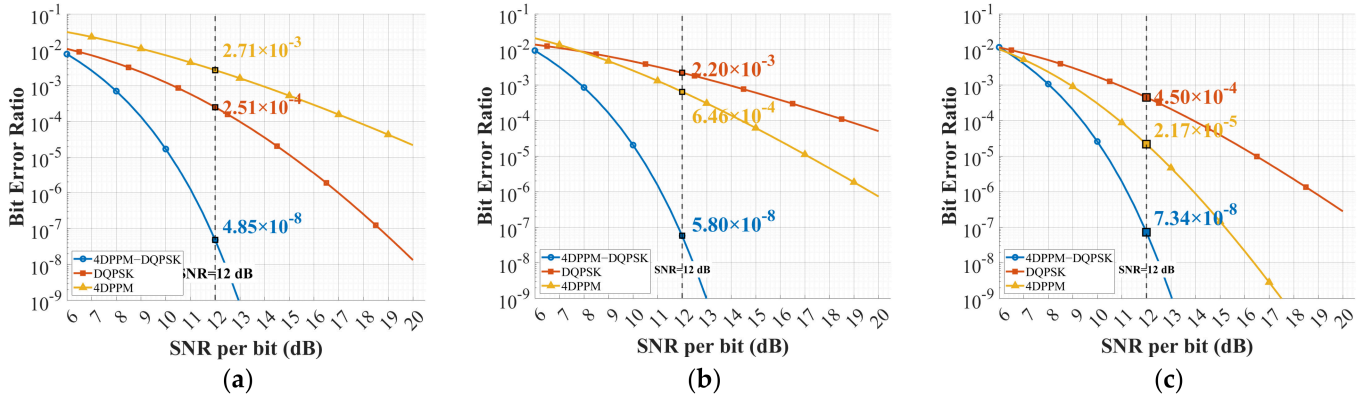


Figure 5. Average BER versus SNR at different propagation distances under weak turbulence (Gamma–Gamma model): (**a**) L = 2000 m, (**b**) L = 5000 m and (**c**) L = 8500 m.

3.2. Log-Normal Distribution

The Log-normal distribution model, derived directly from the Rytov approximation theory, provides high accuracy under weak turbulence conditions. In this model, the received optical intensity I follows a Log-normal distribution with PDF [36]:

$$f(I) = \frac{1}{I \cdot \sqrt{2\pi\sigma_l^2}} \cdot exp\left[-\frac{\left(lnI + \sigma_l^2/2\right)^2}{2\sigma_l^2}\right],\ I \geq 0 \tag{13}$$

$$\sigma_l^2 = \chi \cdot \left(1 + 1.07d^{7/3}\right)^{-1} \tag{14}$$

where parameter χ and d have identical definitions as in the Gamma–Gamma distribution model.

Substituting this PDF into the average BER formulation (9) and maintaining $C_n^2 = 8.2 \times 10^{-15}$ m$^{-2/3}$ for weak turbulence simulation, we calculated the average BER for 4DPPM-DQPSK, as shown in Figure 6. The proposed scheme maintains its performance advantages under the Log-normal model. At SNR = 10 dB and L = 2000 m (Figure 6a), the BER of 4DPPM-DQPSK is 7.62 × 10^{-7}, two orders of magnitude lower than DPPM and four orders of magnitude lower than DQPSK. This superiority persists at longer distances of L = 5000 m (Figure 6b) and L = 8500 m (Figure 6c).

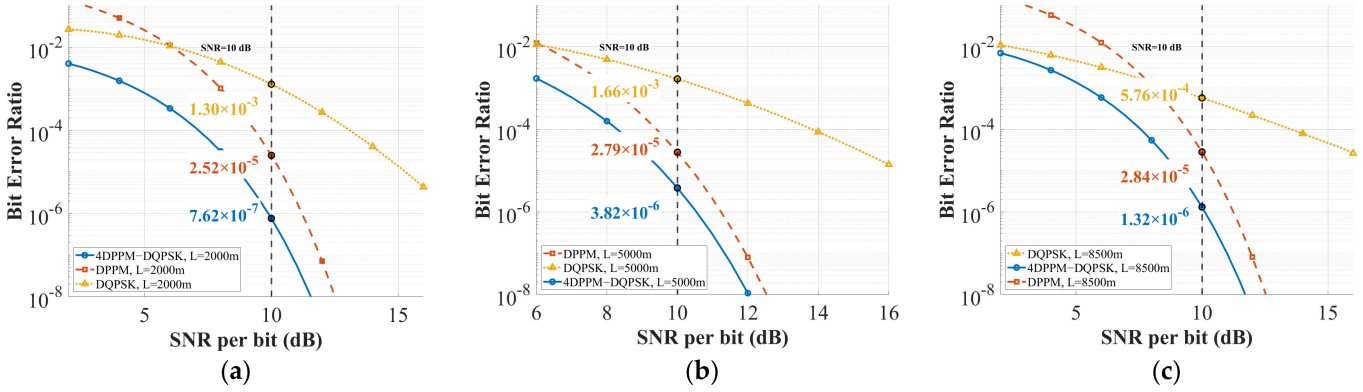


Figure 6. Average BER versus SNR at different propagation distances under weak turbulence (Log-normal model): (**a**) L = 2000 m, (**b**) L = 5000 m and (**c**) L = 8500 m.

3.3. Packet Error Rate

Due to the variable symbol length in DPPM, errors in one time slot can propagate and cause subsequent symbol errors. Therefore, packet error rate (PER) is a more suitable

metric, with the regulation that any error detected within a packet results in the entire packet being erroneous [37]. Assuming N bits per packet and n bits per symbol, each packet contains N/n symbols with the PER defined as [38]:

$$PER \approx \frac{N \cdot L_{av}}{n} \cdot P_{SER} \tag{15}$$

where L_{av} is the average symbol length and P_{SER} is the average slot error rate.

For the hybrid mDPPM-DQPSK format, bits for DQPSK are modulated on the mDPPM pulses. Thus the average symbol length is [39]:

$$L_{av,\, mDPPM-DQPSK} = \frac{2^m + 1}{2} + 2 \tag{16}$$

The P_{SER} under Gamma–Gamma turbulence model is calculated by [40]:

$$P_{SER} = \int_0^\infty P_{se} \cdot f(I) dI \tag{17}$$

where P_{se} is the conditional slot error rate and $f(I)$ is the Gamma–Gamma PDF. Adopting the P_{se} expression given in reference [36,41] and synthesizing these equations, the final PER expression is:

$$PER = \frac{N \cdot L_{av}}{n} \cdot \frac{2(\alpha\beta)^{\frac{\alpha+\beta}{2}}}{\Gamma(\alpha)\Gamma(\beta)} \cdot \int_0^\infty \frac{E(I)}{2(r+1)} \cdot I^{\frac{\alpha+\beta}{2}-1} \cdot K_{\alpha-\beta}\left(2\sqrt{\alpha\beta I}\right) dI \tag{18}$$

where r represents the ratio of the "0" probability to the "1" probability, and $E(I)$ relates to the receiving power and SNR as in reference [36].

We plot the PER curves for 4DPPM-DQPSK in Figure 7 with different packet sizes N. As expected, larger packets (higher N) are more likely to contain errors, resulting in worse PER performance.

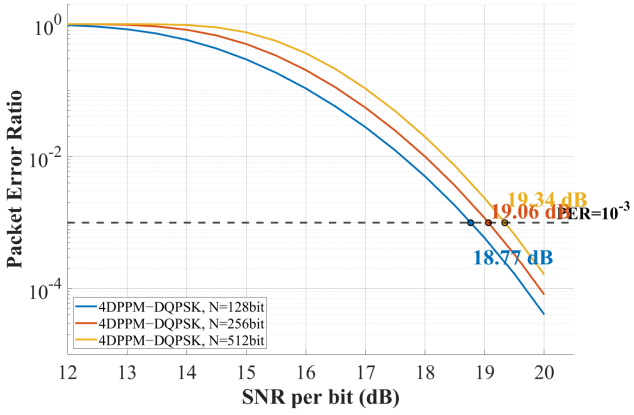


Figure 7. PER curves of 4DPPM-DQPSK for different packet sizes N under Gamma–Gamma turbulence.

We further analyzed PER performances under different turbulence intensities, using the parameter as in the Gamma–Gamma analysis. The PER curves for different transmission distance are shown in Figure 8. PER performance deteriorates with increasing distance. Using a PER of 10^{-3} as a reference, in weak turbulence (Figure 8a), the required SNR ranges from 11.9 dB at L = 1200 m to 14.8 dB at L = 2500 m. Under strong turbulence (Figure 8c), the required SNR is 13.2 dB at L = 1200 m and 15.0 dB at L = 2500 m.

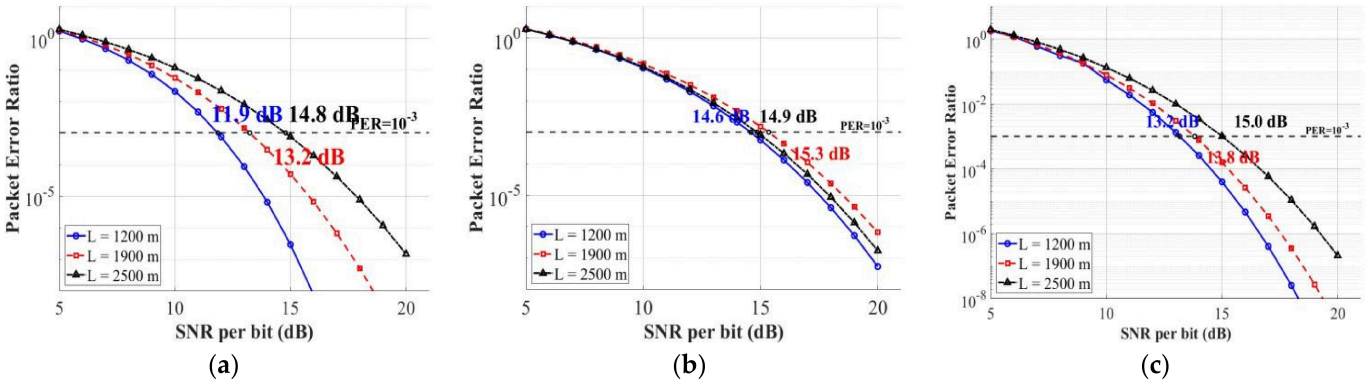


Figure 8. PER performance under different turbulence intensities and transmission distances (Gamma–Gamma model): (**a**) weak turbulence, (**b**) moderate turbulence and (**c**) strong turbulence.

The impact of transmission distance on PER varies with turbulence intensities. In weak and moderate turbulence (Figure 8a,b), PER is strongly affected by transmission distance. In contrast, under strong turbulence (Figure 8c), PER performance is less sensitive to the transmission distance changes, increasing by less than an order of magnitude for the same distance increment. This indicates that in strong turbulence, the turbulence itself is the dominant factor degrading performance, whereas in weaker turbulence, transmission distance plays a more critical role. This insight is valuable for FSO system design, guiding the trade-off between transmission distance and required SNR to maintain consistent performance.

3.4. Phase Robustness and Performance Comparison

To verify the phase robustness advantage of the differential detection scheme, a Monte Carlo simulation is conducted using a Wiener phase noise model. The simulation compares DQPSK (differential detection) against standard QPSK (absolute phase detection) at a symbol rate of 1 Gbaud under laser linewidths of 100 kHz, 500 kHz, and 1 MHz. The results are shown in Figure 9. These results confirm that DQPSK differential detection effectively suppresses slow-varying phase perturbations, where the phase increment between consecutive symbols (~0.025 rad for 100 kHz linewidth at 1 Gbaud) is much smaller than the cumulative absolute phase drift. This supports the claim that the dual-differential mechanism in the proposed mDPPM-DQPSK scheme provides robustness against both intensity scintillation and phase distortion.

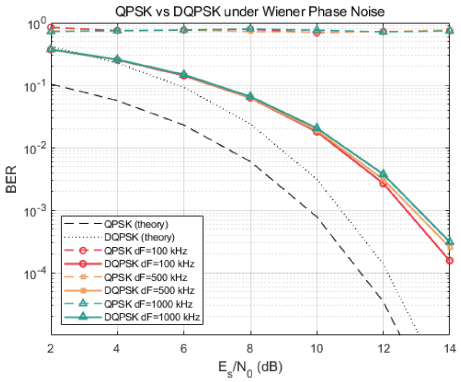


Figure 9. BER comparison of QPSK (absolute detection) and DQPSK (differential detection) under Wiener phase noise with different laser linewidths.

4. Discussion

We compare the proposed mDPPM-DQPSK with existing hybrid schemes, as shown in Table 1. The proposed mDPPM-DQPSK scheme achieves a favorable balance across all

performance dimensions. While PPM-DPSK [24] offers moderate performance at lower complexity, and PPM-QPSK [25] provides high spectral efficiency at the cost of increased phase sensitivity, the dual-differential nature of mDPPM-DQPSK ensures robustness to both intensity scintillation and phase perturbations without requiring carrier recovery, making it well-suited for terrestrial FSO links under varying atmospheric conditions.

Table 1. Comparison of hybrid modulation schemes for FSO links.

Scheme (BWEF)	SE (Bits/Slot)	Intensity Scintillation	Phase Perturbation	Complexity (Rx Requirements)
PPM-DPSK [24] (BWEF = 1.25 for 4PPM)	Moderate	Robust	Moderate	Moderate
PPM-QPSK [25] (BWEF = 1.5 for 4PPM)	High	Robust	Weak (needs CR)	High
mDPPM-DQPSK (proposed, BWEF = 0.625)	High	Robust	Robust (diff. det.)	Moderate

Among existing hybrids, PPM-DPSK achieves moderate turbulence resilience through differential phase encoding but retains PPM's fixed symbol structure, limiting its spectral efficiency (BWEF > 1 for m $\geq$ 4). PPM-QPSK improves spectral efficiency via multi-level phase modulation, yet requires absolute carrier recovery that is susceptible to turbulence-induced phase wander. The proposed dual-differential scheme uniquely combines variable-length pulse positioning with differential phase encoding, simultaneously achieving (i) higher spectral efficiency than standalone DPPM, (ii) phase-noise immunity without carrier recovery, and (iii) a unified BER framework valid under multiple turbulence models—a combination not available in either prior approach. Quantitatively, the proposed scheme achieves a BWEF of 0.625 for m = 4, compared to 1.25 for standalone 4DPPM and 0.5 for DQPSK—a 50% improvement over DPPM. The dual-differential architecture preserves the differential detection advantage that PPM-DPSK introduced for the phase layer [24] while extending it through variable-length pulse positioning that DPSK-based hybrids do not offer. Relative to PPM-QPSK [25], which requires carrier recovery and is sensitive to phase wander, the proposed scheme eliminates the need for carrier recovery entirely through differential encoding in both dimensions, reducing receiver complexity while maintaining robustness to phase perturbations. Furthermore, the proposed scheme provides the first unified BER model valid under both Gamma–Gamma and Log-normal turbulence distributions, whereas prior work [19–21] evaluated performance under only a single turbulence model.

The proposed mDPPM-DQPSK hybrid modulation scheme offers a distinct trade-off among spectral efficiency, power efficiency, and turbulence robustness for terrestrial FSO links. In this section, we discuss the implications of our results, compare with existing approaches, and identify limitations of the current study.

Compared with existing hybrid modulation schemes for FSO systems, the proposed dual-differential approach occupies a unique position. PPM-DPSK [24] offers moderate spectral efficiency with differential phase robustness but retains PPM fixed symbol structure, limiting its SE (BWEF > 1 for $m \geq 4$). PPM-QPSK [25] achieves higher SE through multi-level phase modulation but requires carrier recovery, making it susceptible to turbulence-induced phase wander. Coherent QPSK systems, while offering high sensitivity, demand complex optical phase-locked loops. In contrast, the proposed mDPPM-DQPSK eliminates carrier recovery entirely through dual differential encoding, achieving a BWEF of 0.625 for $m = 4$—a 50% improvement over standalone 4DPPM—while maintaining robustness to both intensity scintillation and phase perturbations.

The simulation results demonstrate BER improvements of several orders of magnitude over standalone DPPM and DQPSK under weak-to-moderate turbulence. However, these gains should be interpreted in the context of the idealized assumptions adopted in the analytical model. The primary limitations of this study include (i) ideal slot synchronization, which neglects synchronization drift in practical DPPM receivers; (ii) AWGN-limited detection without considering thermal noise, shot noise, dark current, or background radiation; (iii) the assumption of statistically independent DPPM and DQPSK errors, which, while justified under the orthogonal detection mechanism, may not fully capture the correlated error behavior in strong turbulence regimes; and (iv) the terrestrial FSO channel model (distances up to 8.5 km) which, while representative of many practical links, does not fully capture the slant-path geometry and altitude-dependent turbulence profiles characteristic of satellite-to-ground links. Future work should address these limitations through experimental validation and more comprehensive channel modeling.

The PER analysis partially addresses the error propagation issue inherent in variable-length DPPM symbols, but a more rigorous treatment of synchronization loss and burst-error statistics would further strengthen the performance characterization. Additionally, the integration of the proposed scheme with channel coding (e.g., LDPC codes) and adaptive modulation techniques [42] represents a promising direction for practical deployment.

5. Conclusions

This paper proposed and analyzed a hybrid mDPPM-DQPSK modulation scheme for terrestrial free-space optical links under atmospheric turbulence. The scheme combines the power efficiency of DPPM with the spectral efficiency of DQPSK through a dual-differential mechanism that mitigates both intensity scintillation and slow-varying phase distortion.

A unified BER model was derived and validated under Gamma–Gamma and Log-normal turbulence channels. Under weak-to-moderate turbulence, the 4DPPM-DQPSK configuration reduces BER by several orders of magnitude compared to standalone DPPM or DQPSK, with a 50% improvement in spectral efficiency over 4DPPM. Phase noise simulations further confirmed that differential detection effectively suppresses slow-varying phase perturbations.

The proposed scheme achieves a favorable balance between capacity, power efficiency, and turbulence robustness without requiring carrier recovery or excessive hardware complexity. These characteristics make it well-suited for terrestrial FSO systems in 6G and LEO satellite networks. Future work may explore several directions to further enhance performance under strong turbulence conditions: (i) integration with advanced channel coding such as low-density parity-check (LDPC) or turbo codes to approach the Shannon limit; (ii) adaptive modulation and power control strategies [42] that dynamically adjust parameters based on real-time turbulence estimation; and (iii) experimental validation of the proposed mDPPM-DQPSK scheme using a hardware testbed under controlled atmospheric conditions to complement the theoretical and simulation results. Furthermore, to rigorously extend the proposed scheme to LEO satellite networks, an appropriate slant-path turbulence model (e.g., the Hufnagel–Valley model) would be required to account for the altitude-dependent refractive index structure constant and zenith-angle-dependent propagation geometry, which differ significantly from the horizontal terrestrial links analyzed in this study.

Author Contributions: Conceptualization and methodology, X.H.; validation and formal analysis, Z.C. and J.W.; investigation and data curation, Z.C.; writing—original draft preparation, X.H.; writing—review and editing, X.H. All authors have read and agreed to the published version of the manuscript.

Funding: This research was funded by the National Natural Science Foundation of China, grant number 62301476 and Postgraduate Research & Practice Innovation Program of Jiangsu Province, grant number SJCX24_2189.

Data Availability Statement: The original contributions presented in this study are included in the article. Further inquiries can be directed to the corresponding author.

Conflicts of Interest: The authors declare no conflicts of interest. The funders had no role in the design of the study; in the collection, analyses, or interpretation of data; in the writing of the manuscript; or in the decision to publish the results.

References

1. Chan, V.W.S. Optical satellite network architecture [Invited tutorial]. *J. Opt. Commun. Netw.* **2024**, *16*, A53–A67.
2. Toyoshima, M. Recent trends in space laser communications for small satellites and constellations. *J. Light. Technol.* **2021**, *39*, 693–699. [CrossRef]
3. Wang, G.; Yang, F.; Song, J.; Han, Z. Free space optical communication for inter-satellite link: Architecture, potentials and trends. *IEEE Commun. Mag.* **2024**, *62*, 110–116. [CrossRef]
4. Zhu, Y.; Xu, G.; Gao, M.; Chu, H.; Song, Z. Average bit-error rate analysis of an inter-satellite optical communication system under the effect of perturbations. *Opt. Express* **2024**, *32*, 36796–36810. [CrossRef] [PubMed]
5. Kolev, D.R.; Carrasco-Casado, A.; Trinh, P.V.; Shiratama, K.; Ishola, F.; Kotake, H.; Nakazono, J.; Saito, Y.; Kunimori, H.; Kubooka, T.; et al. Latest developments in the field of optical communications for small satellites and beyond. *J. Light. Technol.* **2023**, *41*, 3750–3757. [CrossRef]
6. Liu, R.; Zhao, J.; Wan, A. Multi-objective optimization of tracking and control resource scheduling for large-scale LEO satellites. In Proceedings of the 2025 44th Chinese Control Conference (CCC), Chongqing, China, 28–30 July 2025; pp. 2051–2056. [CrossRef]
7. Carrasco-Casado, A.; Do, P.X.; Kolev, D.; Hosonuma, T.; Shiratama, K.; Kunimori, H.; Trinh, P.V.; Abe, Y.; Nakasuka, S.; Toyoshima, M. Intersatellite-link demonstration mission between CubeSOTA (LEO CubeSat) and ETS9-HICALI (GEO satellite). In Proceedings of the 2019 IEEE International Conference on Space Optical Systems and Applications (ICSOS), Portland, OR, USA, 14–16 October 2019; pp. 1–5. [CrossRef]
8. Jiang, Q.; Zhao, K.; Liu, Z.; Meng, X.; Yu, J.; Lin, K.; Hu, M.; Zhao, J. Effect of atmospheric turbulence anisoplanatism on LEO satellite-to-ground laser communications links. *Opt. Express* **2025**, *33*, 40143–40156. [CrossRef] [PubMed]
9. Gao, M.; Xu, G.; Song, Z.; Zhang, Q.; Zhang, W. Performance Analysis of LEO Satellite-Assisted Deep Space Communication Systems. *IEEE Trans. Aerosp. Electron. Syst.* **2025**, *61*, 12628–12648. [CrossRef]
10. Lee, S.-Y.; Jian, Y.-H.; Wei, T.-C.; Chow, C.-W. Beam divergence and atmospheric turbulence resiliency enhancement in free space optical communication with multiple receivers and maximal-ratio combining algorithm. In Proceedings of the 2025 Optical Fiber Communications Conference and Exhibition (OFC), San Francisco, CA, USA, 30 March–3 April 2025; pp. 1–3.
11. Ata, Y.; Gökçe, M.C.; Baykal, Y. Mitigation of atmospheric turbulence on up and downlink optical communication systems using receiver diversity and adaptive optics. *Opt. Quantum Electron.* **2022**, *54*, 659. [CrossRef]
12. Li, M.; Cvijetic, M.; Takashima, Y.; Yu, Z. Evaluation of channel capacities of OAM-based FSO link with real-time wavefront correction by adaptive optics. *Opt. Express* **2014**, *22*, 31337–31346. [CrossRef]
13. Zhang, Z.; Jia, S.; Shao, W.; Gao, D.; Wang, W.; Si, J.; Xie, X. Turbulence compensation based on pix-2-pixGAN for the free-space optical communication of orbital angular momentum multiplexing. *Appl. Opt.* **2025**, *64*, A1–A11. [CrossRef]
14. Yu, H.; Li, L.; Hou, Y.; Li, Y.; Yin, C.; Gao, C.; Fu, S. Deep learning-based prediction of atmospheric turbulence toward satellite-to-ground laser communication. *Opt. Lett.* **2025**, *50*, 273–276. [CrossRef]
15. Liu, N.; Ju, C.; Wang, D.; Wang, D.; Xie, P. Multi-aperture coherent digital combining based on complex-valued MIMO 2N×2 adaptive equalizer for FSO communication. *J. Light. Technol.* **2023**, *41*, 5983–5990. [CrossRef]
16. Zhang, M.; Wei, Z.; Lei, T.; Wu, R.; Heng, T.; Ma, Y.; Du, L.; Yuan, X. High-Speed Free-Space Optical Communication Using Mode Demultiplexers and Coherent Beam Combining. *J. Light. Technol.* **2025**, *43*, 7590–7596. [CrossRef]
17. Palitharathna, K.W.S.; Suraweera, H.A.; Godaliyadda, R.I.; Herath, V.R.; Thompson, J.S. Average rate analysis of cooperative NOMA aided underwater optical wireless systems. *IEEE Open J. Commun. Soc.* **2021**, *2*, 2292–2310. [CrossRef]
18. Bhowal, A.; Kshetrimayum, R.S. Transmit laser selection for dual hop decode and forward UOWC cooperative communication. In Proceedings of the 2020 IEEE Wireless Communications and Networking Conference (WCNC), Seoul, Republic of Korea, 25–28 May 2020; pp. 1–6.
19. Robinson, B.S.; Boroson, D.M.; Burianek, D.A.; Murphy, D.V. Overview of the lunar laser communications demonstration. In Proceedings of the SPIE Photonics West, San Francisco, CA, USA, 22–27 January 2011; Volume 7923, p. 792302.

20. Robinson, B.S.; Shih, T.; Khatri, F.I.; Boroson, D.M.; Guldner, O.; Constantine, S.; Torres, J.; Yarnall, T.M.; Hubbard, W.; Geisler, D.J.; et al. Laser communications for human space exploration in cislunar space: ILLUMA-T and O2O. In Proceedings of the SPIE Photonics West, San Francisco, CA, USA, 27 January–1 February 2018; Volume 10524, pp. 231–235. [CrossRef]
21. Biswas, A.; Boroson, D.; Edwards, B. Mars laser communication demonstration: What it would have been. In Proceedings of the SPIE Photonics West2006, San Jose, CA, USA, 21–26 January 2006; Volume 6105, p. 610502.
22. Ata, Y.; Baykal, Y.; Gökçe, M.C. M-ary pulse position modulation performance in non-Kolmogorov turbulent atmosphere. *Appl. Opt.* **2018**, *57*, 7006–7011. [CrossRef]
23. El-Fikky, A.A.; Ghazy, A.S.; Khallaf, H.S.; Mohamed, E.M.; Shalaby, H.M.H.; Aly, M.H. On the performance of adaptive hybrid MQAM-MPPM scheme over Nakagami and log-normal dynamic visible light communication channels. *Appl. Opt.* **2020**, *59*, 1896–1906. [CrossRef]
24. Shin, W.H.; Lee, J.W.; Ha, I.H.; Han, S.-K. Data rate enhancement of free space optical communication using pulse positioned differential phase shift keying. *Opt. Express* **2021**, *29*, 26039–26047. [CrossRef]
25. Song, J.; Yuan, M.; Li, Y.; Qiu, J.; Hong, X.; Guo, H.; Yang, Z.; Wu, J. Real-time FPGA prototyping of high sensitivity 15Gbps 4PPM-QPSK receiver. In Proceedings of the 49th European Conference on Optical Communications (ECOC 2023), Glasgow, UK, 1–5 October 2023; pp. 357–360. [CrossRef]
26. Guan, C.; Zhang, Z.; Jia, F.; Zhao, Y. Laser Heterodyne Detection Based on Photon Time–Domain Differential Detection Avoiding the Effect of Decoherence Phase Noise. *Sensors* **2023**, *23*, 9435. [CrossRef]
27. Caplan, D.O. Laser communication transmitter and receiver design. *J. Opt. Fiber Commun. Rep.* **2007**, *4*, 225–362. [CrossRef]
28. Proakis, J.G. *Digital Communications*, 4th ed.; McGraw-Hill: Boston, MA, USA, 2001.
29. Barakat, R. Sums of independent lognormally distributed random variables. *J. Opt. Soc. Am. A* **1976**, *66*, 211–216. [CrossRef]
30. Liu, X.; Chandrasekhar, S.; Leven, A. Self-coherent optical transport systems. In *Optical Fiber Telecommunications V B*; Academic Press: New York, NY, USA, 2008; pp. 131–177.
31. Hamid, S. Performance Evaluation of Optically Preamplified M-Ary PPM Systems for Free-Space Optical Communications. Master's Thesis, American University of Sharjah, Sharjah, United Arab Emirates, 2013.
32. Gelaw, Z.L.; Annamalai, P.; Ayalew, H.D. Performance Analysis of Gray-Coded DP-16QAM MIMO-FSO Systems With Coherent Detection and DSP Techniques. *J. Comput. Netw. Commun.* **2025**, *2025*, 4243779. [CrossRef]
33. Liu, X.; Wood, T.H.; Tkach, R.W.; Chandrasekhar, S. Demonstration of record sensitivities in optically preamplified receivers by combining PDM-QPSK and M-ary pulse-position modulation. *J. Light. Technol.* **2011**, *30*, 406–413. [CrossRef]
34. Andrews, L.C.; Andrews, L.C. New mathematical model for the intensity PDF of a laser beam propagating through turbulent media. In Proceedings of the SPIE Defense + Security, Orlando, FL, USA, 5–9 April 1999; Volume 3706, pp. 156–167.
35. Li, M.; Zhang, P.; Wang, T. Evaluation of atmospheric coherent length of free-space optical links by using phase fluctuation. *Opt. Express* **2024**, *32*, 7243–7253. [CrossRef]
36. Andrews, L.C.; Phillips, R.L.; Hopen, C.Y. *Laser Beam Propagation Through Random Media*, 2nd ed.; SPIE Press: Bellingham, WA, USA, 2005; Chapter 8, Equations (8)–(86).
37. Kiasaleh, K. Performance of APD-based PPM free-space optical communication systems in atmospheric turbulence. *IEEE Trans. Commun.* **2005**, *53*, 1455–1461. [CrossRef]
38. Wang, H.; Xu, J.; Sun, X.; Hu, H.; Wu, X.J. Performance analysis of MIMO-FSO systems based on PPM modulation and Gamma-Gamma distribution model. *Syst. Eng. Electron.* **2012**, *34*, 385–390.
39. Liu, H.; Liao, R.; Sun, J.; Liu, L. Performance analysis of new hybrid pulse modulation scheme in optical wireless system. *Acta Opt. Sin.* **2015**, *35*, 0706004. [CrossRef]
40. Han, L.; Wang, Q.; Shida, K. Performance of free space optical communication over Gamma-Gamma atmosphere turbulence. *Infrared Laser Eng.* **2011**, *40*, 1318–1322.
41. Wang, T.; Hao, Z.; Li, H.; Zhan, W.; Li, R. Error rate performance of differential multi-pulse position modulation. *Clust. Comput.* **2019**, *22*, 14615–14623.
42. Feng, S.; Li, N.; Liu, K.; Li, B.; Dong, C.; Wu, Q. A Cross Q-Learning Assisted Resource Allocation for User-Centric Optical Wireless Communication Networks. *IEEE Trans. Green Commun. Netw.* **2025**, *9*, 2264–2278. [CrossRef]

Disclaimer/Publisher's Note: The statements, opinions and data contained in all publications are solely those of the individual author(s) and contributor(s) and not of MDPI and/or the editor(s). MDPI and/or the editor(s) disclaim responsibility for any injury to people or property resulting from any ideas, methods, instructions or products referred to in the content.